Simultaneous Nanoindentation and Electron Tunneling through Alkanethiol Self-Assembled Monolayers

Vincent B. Engelkes and C. Daniel Frisbie*

Department of Chemical Engineering and Materials Science, University of Minnesota,
421 Washington Avenue Southeast, Minneapolis, Minnesota 55455

Electrical tunnel junctions consisting of alkanethiol molecules self-assembled on Au-coated Si substrates and contacted with Au-coated atomic force microscopy tips were characterized under varying junction loads in a conducting-probe atomic force microscopy configuration. Junction load was cycled in the fashion of a standard nanoindentation experiment; however, junction conductance rather than probe depth was measured directly. The junction conductance data have been analyzed with typical contact mechanics (Derjaguin−Müller−Toporov) and tunneling equations to extract the monolayer modulus ($\sim$50 GPa), the contact transmission ($\sim 2 \times 10^{-6}$), contact area, and probe depth as a function of load. The monolayers are shown to undergo significant plastic deformation under compression, yielding indentations $\sim$7 Å deep for maximum junction loads of $\sim$50 nN. Comparison of mechanical properties for different chain lengths was also performed. The film modulus decreased with the number of carbons in the molecular chain for shorter-chain films. This trend abruptly reversed once 12 carbons were present along the backbone.

Introduction

Many reports describe the tunneling conductance of self-assembled monolayers (SAMs) on metallic electrodes in various junction configurations.[1−8] The primary aim of these reports is to relate the conductance to properties of the molecules including molecular length,[5,7,9] electronic structure,[6,10] and the nature of the electrode−molecule contacts.[1,4,5,11] Each junction configuration offers the ability to perform conductance measurements while controlling external or environmental parameters. The nanopore junction of Zhou et al.,[12] for example, offers an advantage over other configurations for characterization of the temperature dependence of molecular junctions. Junctions formed under solution provide the ability to probe electrochemical gating effects on conductance.[13] Mechanically controllable break junctions enable single-molecule measurements.[8] The strengths of conducting-probe atomic force microscopy (CP-AFM) include the ability to quickly characterize the electrical properties of junctions using a variety of metal contacts and the ability to precisely control applied loads (sub-nanonewton) in the junction.

This report presents a detailed description of low-bias conductance measurements as a function of load for junctions composed of Au−S−$(CH_2)_{n-1}$−CH_3/Au sandwich structures. The various alkanethiol molecules (denoted C_n, where n is the number of carbon atoms in the molecular chain) form self-assembled monolayers on the surface of flat, template-stripped Au-coated Si substrates. The terminal methyl groups of the monolayer are contacted with a Au-coated AFM tip to complete the CP-AFM junction (Figure 1). The conductance−load data are analyzed to infer mechanical and electronic properties of the junctions. These properties include the film modulus, contact transmission function, and degree of plastic deformation and are determined for four different lengths of alkanethiol chains

Figure 1. Schematic illustration of a molecular junction formed using CP-AFM and the AFM setup for measuring load-dependent behavior. The Si/Au/monolayer substrate is moved up and down with the z-piezo, such that the tip presses into and out of contact with the monolayer over a range of applied loads. External electrometers are used to apply voltage to the tip (V_{ap}), measure junction current (I), cantilever deflection (V_1), and monitor the height of the substrate (V_2).

(n = 6, 8, 10, and 12). The mechanical parameters scale in a predictable fashion; namely, as the chains become longer, the monolayers become less stiff. While this trend remains true for the short-chain films, an abrupt increase in the stiffness is observed between monolayers of C_{10} and C_{12}, which confirms

* Author to whom correspondence should be addressed. E-mail: frisbie@cems.umn.edu.

10012 *J. Phys. Chem. B, Vol. 110, No. 20, 2006*

Engelkes and Frisbie

previous observations that a distinct change in the packing (increase in crystallinity) of short-chain and long-chain monolayers occurs somewhere between the lengths of C_8 and C_{12} in SAM films.[14] The plastic deformation is observed to be essentially constant with chain length. An electronic parameter, the contact transmission function, also exhibits little dependence on chain length. Overall, these measurements provide a more detailed understanding of the physical properties of CP-AFM tunnel junctions, which will be useful as the technique is applied to a broader range of molecular systems.

Experimental Section

Materials. Gold nuggets (99.999% pure) were obtained from Mowrey, Inc. (St. Paul, MN). Evaporation boats and chromium evaporation rods were purchased from R. D. Mathis (Long Beach, CA). Aluminum shot (99.999% pure) was obtained from Alfa Aesar (Ward Hill, MA). Silicon (100) wafers were purchased from WaferNet (San Jose, CA). V-shaped AFM cantilevers and tips (model DNP) were obtained from Digital Instruments. Ethanol (reagent alcohol) and cyclohexane were purchased from Fisher Scientific. Alkanethiol molecules were obtained from Aldrich. EPO-TEK 377 epoxy was purchased from Epoxy Technology (Billerica, MA).

Sample and Tip Preparation. Silicon substrates and contact mode AFM tips were coated with metal using a Balzers thermal metal evaporator at a base pressure of $\sim 2 \times 10^{-6}$ Torr. Tips were coated with 1500 Å of Au at a rate of 1 Å/s after the deposition of a 50 Å Cr adhesion layer. Nearly all substrates were coated only with Au and template-stripped according to the procedure of Blackstock et al.[15] First, 5000 Å of Au was deposited onto a clean Si wafer. One square centimeter pieces of Si were then glued to this layer using epoxy, with the polished side to the Au surface. This sandwich structure was then baked at ~ 120 C° for 1 h or until cured. Substrates were pried away using a razor blade or tweezers, cleaving the Au/Si interface. Monolayers were self-assembled on all Au substrates by immersion in ~ 0.5 mM solutions of the desired molecule in ethanol for at least a few hours. Fresh batches of tips and monolayers were made after about 4 or 5 days. One sample of Al-coated Si was made in a similar manner as the tips without the Cr adhesion layer. These surfaces were about 10 times rougher than the template-stripped Au substrates; however, template-stripped Al substrates could not be made because the Al bonded strongly to the Si. The Al substrate was allowed to sit in ambient conditions for a few hours, after which it was assumed that a native thin film of Al_2O_3 had formed.

Tip Radius and Force Constant Determination. Tip radii were estimated by imaging microfabricated Si spikes on a substrate purchased from Micromasch, Inc. These measurements indicated that the metal-coated tips all had radii of approximately 20 nm, which was the value used in our modeling calculations described later.

Cantilever force constants were determined by the thermal fluctuation method using an EG&G model 7260 lock-in amplifier.[16,17] The cantilever was mounted in the atomic force microscope, and the laser was aligned so that the power spectral density (PSD) could be directly measured from the deflection voltage on the AFM photodiode. The mean square deflection of the cantilever ($\langle z^2 \rangle$) due to thermal fluctuation was determined by integrating the first mode in the PSD (about $50-100$ PSD traces were averaged together) followed by a division by 0.86. (It was assumed that 97% of the total power was partitioned into the first mode and that the photodiode measured a 89%

demagnification of the deflection of this mode.[17]) The force constant, k, was then determined from the following equation

$$k = \frac{k_B T}{\langle z^2 \rangle} \qquad (1)$$

where k_B is the Boltzmann constant and T is the temperature. This method ensured that when different cantilevers were used valid comparisons could be made for load-dependent measurements.

Conductance versus Load Measurements. Electrical junctions were formed by bringing a metallized tip into contact with a monolayer-coated substrate using a Digital Instruments MultiMode AFM (Figure 1). Measurements under cyclohexane were performed using a specially designed liquid cell for the MultiMode from Veeco Instruments, Inc. To measure the load in the junction, the tip was first brought into contact with the substrate, and a force−distance curve was generated. This curve represented the photodiode signal (V_1) versus distance traversed by the z-piezo and substrate (calculated from V_2 and the calibration of the piezo). It was assumed that little deformation of the film occurred relative to the distance traveled by the substrate, such that the z-piezo signal equaled the deflection of the cantilever. Therefore, the slope (S) of the force−distance trace provided a ratio of cantilever deflection to photodiode signal (units of nm/V). Applied load (P_{ap}) could be then calculated directly from the photodiode signal using the following equation

$$P_{ap} = kSV_1 \qquad (2)$$

where k is the force constant as determined by eq 1.

Once calibration was complete, junction current and applied load were measured simultaneously while the tip was cycled slowly (~ 20 nm/s) through a force−distance trace using the NanoScope software. The tip was held at a constant potential (V_{ap}) of 0.2 V, and the junction current (I) was measured using a Keithley 6517 source/measure unit. The cantilever deflection (V_1) and z-piezo height (V_2) were recorded using Keithley 2000 electrometers directly connected to the microscope's signal access module. For the MultiMode system, these were the "In 0" and "LV Z" BNC voltage outputs, respectively. Multiple force−distance traces of this nature were recorded and averaged by binning the data over small load intervals. All external electrometers were controlled using LabVIEW software.

Results and Discussion

Conductance versus Load. The force−distance trace (Figure 2A) consists of two regimes, extension (loading) and retraction (unloading), as indicated by the sloped arrows. The sample approaches the tip during extension, and once in contact (position i), the junction undergoes increasing compression (i → ii). The compression is reduced during the retraction regime (ii → iii) until the tip is removed from contact (position iii), displaying a large pull-off or adhesion force (P_{ad}). Figure 2A shows raw data from a representative force−distance trace collected on a decanethiol (C_{10}) monolayer in air including the distance moved by the z-piezo (sample height), applied load, and the conductance. The applied load is acquired from the AFM photodiode voltage (V_1) and converted to load units using eq 2, resulting in data that has an arbitrary zero value. To determine the zero-point load, a line is fit through the data where the tip is not in contact (i.e., prior to position i and after position iii) and subtracted from the data. The conductance is determined
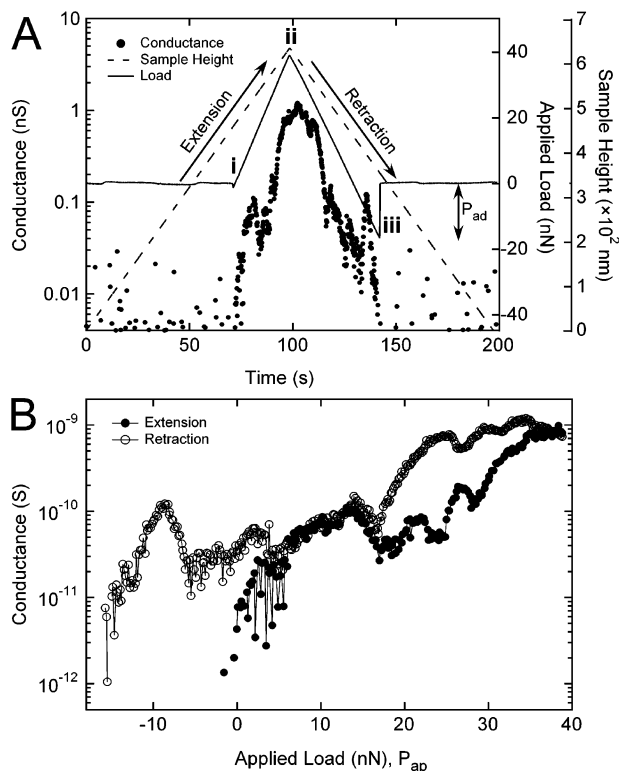
Nanoindentation and Tunneling through SAMs

J. Phys. Chem. B, Vol. 110, No. 20, 2006 **10013**

Figure 2. (A) Representative data from a force−distance curve for a C_{10} junction in air including *z*-piezo/sample height (dashed line), applied load (solid line), and conductance (●) versus time. The extension regime (loading) consists of the period of time where the sample approaches the tip, engages the surface (i) and compression in the junction increases. At position ii the piezo reverses direction. During the retraction regime (unloading), the sample withdraws from the tip, and junction compression is reduced. At position iii, the tip snaps off the surface due to an adhesive force, P_{ad}. (B) Extension (●) and retraction (○) data from panel A recast as conductance versus applied load.

Figure 3. (A) Average conductance data for 10 different tips on C_{10} films in air with a P_{max} of ∼30 nN. The conductance is always greater during the unloading regime than during the loading regime. The inset shows the ratio of unloading to loading conductance (defined as the hysteresis ratio), which is greater than one and approaches one at P_{max}. (B) Conductance data collected with one tip on a C_{10} film under cyclohexane. Hysteresis in the conductance is still observed despite the elimination of adhesion forces. The inset shows the ratio of unloading to loading conductance, which is again greater than one and approaches one at P_{max}. The typical duration for one loading−unloading cycle was ∼20 s.

by dividing the measured current (*I*) by the applied voltage (V_{ap}), which is held constant at 0.2 V. Figure 2B recasts the same set of data as conductance versus applied load, distinguishing the extension (filled circles) and retraction regimes (open circles). The maximum applied load (P_{max}) and the loading rate are controllable parameters.

Hysteresis. The data in Figure 2B indicate that higher conductance is observed during unloading than during loading. That is, for a particular applied load, the conductance observed on the retraction trace is larger than that on the extension trace. This observation of conductance hysteresis is very reproducible and occurs for all experimental conditions under which SAM junctions are tested. Figure 3A is a plot of average conductance versus applied load for C_{10} junctions in air, which clearly illustrates that larger conductance values are measured during unloading. The average is performed on data acquired with 10 different tips and with an average applied P_{max} of ∼30 nN. The inset of Figure 3A displays the hysteresis ratio (unloading conductance divided by loading conductance), which remains greater than one until P_{max} is reached, at which point it equals one. Conductance−load traces acquired under cyclohexane also exhibit a similar amount of hysteresis as observed in Figure 3B. This is an important observation, because adhesion forces are almost entirely eliminated under solvent such that the hysteresis in conductance cannot result from so-called adhesion hysteresis in which adhesion alone causes an increase in the contact area upon retraction.[18] The observed hysteresis must be attributed to a different effect.

Three types of experiments were performed to determine the cause of the observed conductance−applied load hysteresis. These included experiments where the loading rate was varied, the maximum applied load was varied, and the monolayer was replaced with a native Al_2O_3 layer. Loading rate was varied primarily to test whether the monolayer exhibits a viscoelastic response to compression. A second time-dependent consideration is the effect of capacitance, i.e., charging of the circuitry during the time scale of the measurement. For instance, if the circuitry behaves as a leaky capacitor, then faster force−distance traces would not allow transient capacitive charging currents to decay prior to completion of the trace. This would increase the size of the hysteresis loop; however, higher conductance would be expected on the loading trace, which is not observed. If the junction behaves viscoelastically, then faster loading rates should reduce observed hysteresis because the monolayer would behave more elastically at faster rates. To check for this trend, data collected on C_{10} monolayers in air with a constant P_{max} of ∼30 nN were separated according to loading rate and compared. Lines were fit to log plots of the hysteresis ratio versus loading rate for a set of applied loads between 0 and 30 nN. For example, Figure 4A is one such plot of hysteresis ratio evaluated at 10 nN of applied load versus loading rate. No trend in the hysteresis is observed as a function of loading rate as indicated by the weak slope (0.01) and r^2 value (0.00). The inset of Figure 4A is a plot of the slope (as determined for $P_{ap} = 10$ nN in the main panel) evaluated for other values of P_{ap} over the entire loading range. Again, the slope hovers around zero, and the
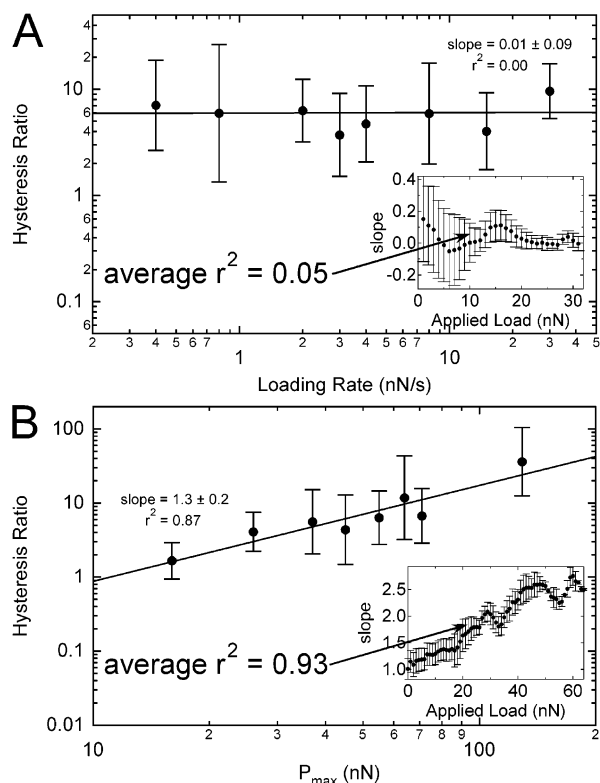
Figure 4. (A) Hysteresis ratio evaluated at 10 nN of applied load versus loading rate for C_{10} monolayers. No trend is observed as noted by the weak slope and r^2 value. The inset shows that the slope of such plots over the entire applied load range is very near zero and the average r^2 value is only 0.05. (B) Hysteresis ratio at 10 nN of applied load versus P_{max} for C_{10} monolayers. The hysteresis is observed to increase with P_{max} with a strong r^2 value (0.87). The inset again shows that the slope is positive over the entire applied load range with a very strong average square correlation coefficient of 0.93.

average r^2 value for all of the fits is 0.05, indicating that the monolayer is not deforming in a time-dependent fashion.

Force−distance traces obtained with various P_{max} values show definite differences in hysteresis. Figure 4B is a log plot of the hysteresis ratio at 10 nN of applied load versus the approximate P_{max} value for data collected on C_{10} monolayers in air. The hysteresis increases with increasing P_{max} and is strongly correlated with an r^2 value of 0.87. As in panel A, the inset displays the slope evaluated for other P_{ap} values throughout the loading range. The slope exhibits the same positive trend for all applied loads with an average r^2 value of the fits equal to 0.93. This behavior is consistent with the assertion that the monolayer film is deformed both elastically and plastically during loading and that only partial (elastic) recovery occurs during unloading. The hysteresis is not rate-dependent but rather dependent on the amount of plastic deformation that is imparted on the film, which can be increased by increasing P_{max}. Similar load-depth hysteresis on monolayers has been observed by others.[19]

Figure 5 displays conductance data for both loading and unloading acquired on a native Al_2O_3 film. The Al_2O_3 is much harder (yield strength, 15.4 GPa; Young's modulus, 530 GPa)[20] than the organic monolayer and should not undergo much deformation. The hardness of Al_2O_3 coupled with the fact that no tangible hysteresis is observed in the data of Figure 5 further confirms that the hysteresis (in Figure 3) observed for monolayer films is primarily due to plastic deformation of the monolayer during loading. Therefore, the loading and unloading cycle is very similar to a nanoindentation experiment of the SAM film.
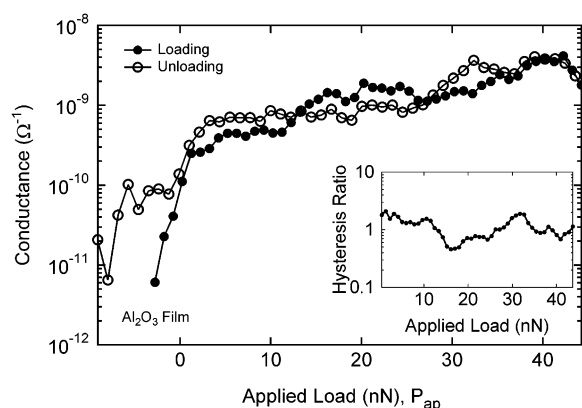
Figure 5. Conductance data collected with one tip on a native Al_2O_3 film in air. No significant difference is observed between loading and unloading. The inset shows the ratio of unloading to loading conductance, which is essentially equal to unity for all loads. This suggests no plastic deformation occurs within the film. Plastic deformation does not occur for the tip up to a stress of ∼200 MPa.

However, in typical nanoindentation experiments, plots of load versus penetration depth are generated.[21] Here, plots of conductance versus load are generated first, and the conductance is probably not a simple function of displacement. The following sections will attempt to transform the conductance−load data into more conventional plots of load versus indentation depth.

Modeling SAM Conduction as a Function of Load. It is well-known that conduction through aliphatic SAMs is dominated by quantum-mechanical tunneling. Therefore, the conductance (G) is described as a product of factors that account for electronic coupling between electrodes. These factors generally simplify into an equation that has the following form

$$G = G_0 \exp(-\beta t) \qquad (3)$$

where G_0 is the contact conductance, t is the thickness of the junction, and β is the thickness attenuation factor that primarily depends on the electronic structure of the monolayer. For junctions containing aliphatic films such as C_{10} monolayers, the reported value of β is ∼0.9 Å^{-1}.[1,3,4] The parameters of eq 3 functionally depend on the applied load for the experiments contained in this paper. For example, the thickness (t) of the junction is a variable that is reduced upon compression and that exponentially affects the conductance. The contact conductance (G_0) is also expected to scale linearly with the contact area and is likely a function of pressure as the electronic overlap between monolayer and tip orbitals is improved. It is also possible that the β value may be dependent on pressure.

To more accurately model conduction and specify values for the factors in eq 3, the Landauer equation is used.[22] This equation states that junction conductance equals the quantum unit of conductance ($2e^2/h$) times the transmission probability of the junction and the number of modes of propagation (N), where e is the unit charge (1.6×10^{-19} C) and h is Planck's constant (6.626×10^{-34} J s). In the case of a monolayer, the number of modes is simply the number of molecules in the junction, assuming that intermolecular coupling is weak and the molecules behave as independent resistors. Generally, we can divide the transmission of the junction into factors that account individually for the contacts (T_0) and the molecular chain (T_{mol}). Hence, the exponential factor in eq 3 is T_{mol} such that the equation can be rewritten
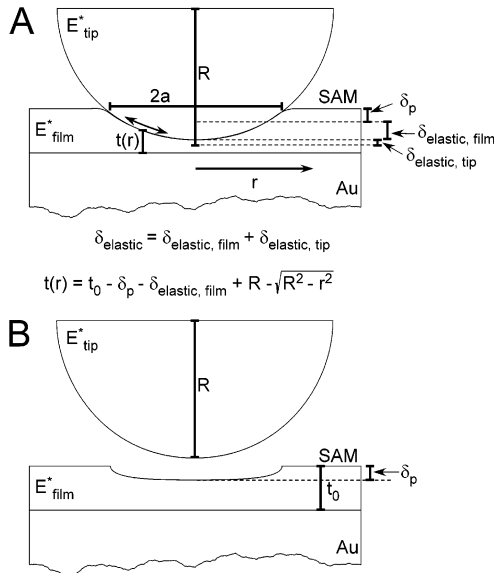
$$G = \frac{2e^2}{h} N T_0 \exp(-\beta t) \qquad (4a)$$

Nanoindentation and Tunneling through SAMs

J. Phys. Chem. B, Vol. 110, No. 20, 2006 **10015**

Figure 6. (A) Schematic representation (not drawn to scale) of a tip of radius, R, compressing a SAM film defining the contact radius (a), radial axis (r), and elastic deformation (δ_{elastic}). The elastic deformation is displayed as divided between the film (δ_{film}) and the tip (δ_{tip}). (B) Illustration of the junction after compressive force is alleviated. Plastic deformation (δ_{p}) remains (also shown in panel A) such that the film thickness after the experiment is thinner than the pristine film (t_0). E_{tip}^* and E_{film}^* represent the tip and film moduli, respectively.

where

$$\frac{2e^2}{h} N T_0 \equiv G_0 \tag{4b}$$

$$\exp(-\beta t) \equiv T_{\text{mol}} \tag{4c}$$

Equation 4a can be further specified to account for changes in contact area and the amount of elastic compression in the film. The thickness of the junction is reduced by the compression in the film, and it is also dependent on the radial position in the contact circle ($t(r)$, Figure 6). It is imperative to include this radial dependence due to the curvature of the tip (at least to low order) because the thickness has a strong effect on the conductance. Therefore, the thickness is expressed as a function of r (the radial axis of the contact circle), and the conductance is determined by an integral in cylindrical coordinates

$$G = \frac{2e^2}{h} \sigma T_0 \int_0^{2\pi} \int_0^a \exp(-\beta t(r)) r \, dr \, d\theta \tag{5}$$

where σ is the surface coverage of molecules and a is the contact radius. The thickness (t) of the film involves three parameters: the original undeformed thickness (t_0), the plastic deformation (δ_{p}), and the elastic deformation ($\delta_{\text{elastic,film}}$). It is easiest to only consider the unloading trace to begin with, because only the elastic deformation is variable in this regime. However, it is noted that a constant amount of plastic deformation exists (δ_{p}), which must be included the model.

Introduction of the film deformation requires some subtle discussion. It is not conclusive whether conduction occurs along the backbone of the molecule (through-bond), directly through space, or a combination of these two possible pathways. While inclusion of the deformation seems to indicate acceptance of a through-space model, this is not necessarily true. For instance, as the film is compressed, the tip may no longer probe the terminus of the molecules in the film but rather units along the

length of the backbone. It is difficult to discern between this effect and the effect of through-space transport; therefore, both situations are assumed to be accounted for with the inclusion of the elastic deformation, and the β-value is considered a conglomerate of β-values for each case.

Values for the contact radius (a) and elastic deformation at the center of the contact circle (δ_{elastic}) can be calculated using the equations of Hertzian mechanics where R is the radius of the tip and P is the junction load.[23] E^* is defined as the reduced elastic modulus where E_{film}, ν_{film} and E_{tip}, ν_{tip} are the Young's modulus and Poisson's ratio of the monolayer film and tip, respectively

$$a^2 = \left(\frac{3R}{4E^*}\right)^{2/3} P^{2/3} \tag{6a}$$

$$\delta_{\text{elastic}} = \left(\frac{9}{16R}\right)^{1/3}\left(\frac{1}{E^*}\right)^{2/3} P^{2/3} \tag{6b}$$

$$E^* = \left(\frac{1 - \nu_{\text{film}}^2}{E_{\text{film}}} + \frac{1 - \nu_{\text{tip}}^2}{E_{\text{tip}}}\right)^{-1} \equiv \left(\frac{1}{E_{\text{film}}^*} + \frac{1}{E_{\text{tip}}^*}\right)^{-1} \tag{6c}$$

Equation 6b describes the total elastic deformation at the center of the contact circle, i.e., the sum of the deformation in the film ($\delta_{\text{elastic,film}}$) and in the tip ($\delta_{\text{elastic,tip}}$). To estimate $\delta_{\text{elastic,film}}$, a proportion of E^* is chosen as determined from eq 6c

$$\delta_{\text{elastic,film}} = \frac{E^*}{E_{\text{film}}^*} \delta_{\text{elastic}} \tag{7}$$

Therefore, the film thickness during unloading at the center of the contact circle is equal to the undeformed film thickness (t_0) minus the final induced plastic deformation (δ_{p}) and the elastic film deformation ($\delta_{\text{elastic,film}}$). The radial dependence of the film thickness is estimated simply by the profile of a hemispherical tip (Figure 6)

$$t(r) = t_0 - \delta_{\text{p}} - \delta_{\text{elastic,film}} + R\left(1 - \sqrt{1 - \left(\frac{r}{R}\right)^2}\right) \tag{8}$$

Equation 8 assumes that $\delta_{\text{elastic,tip}}$ is small compared to R. Substitution of eqs 6–8 into eq 5 and integration yield the following functional form of G as a function of P for the unloading data

$$G(P) = C \frac{4\pi e^2 \sigma}{h\beta^2} \exp\left(\beta\left(\frac{3}{4}\left(\frac{E^*}{R E_{\text{film}}^{*3}}\right)^{1/2} P\right)^{2/3}\right) \times$$
$$\left\{\beta R - 1 - \left(\beta R\sqrt{1 - \left(\frac{3P}{4R^2 E^*}\right)^{2/3}} - 1\right) \times \right.$$
$$\left. \exp\left(\beta R\left(\sqrt{1 - \left(\frac{3P}{4R^2 E^*}\right)^{2/3}} - 1\right)\right)\right\} \tag{9a}$$

where

$$C \equiv T_0 \exp(-\beta(t_0 - \delta_{\text{p}})) \tag{9b}$$

In this equation, C and E_{film}^* are fitting parameters.

Equation 9a does not include a dependence of β on P because our data suggest that it probably does not change considerably. Figure 7A displays representative conductance versus applied load data for octanethiol (C_8), decanethiol (C_{10}), and dodecanethiol (C_{12}) monolayers in air. The β-value (Figure 7B) is conventionally determined by the slope of a linear least-squares fit to the logarithm of the conductance versus number of carbons
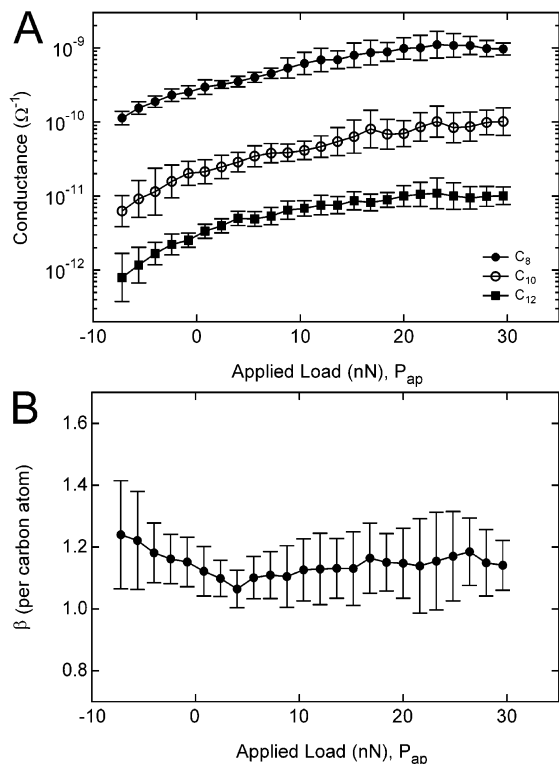
Figure 7. (A) Conductance versus applied load data (unloading only) for monolayers of C_8 (●), C_{10} (○), and C_{12} (■) collected with a representative tip. (B) β-value as calculated from the data in panel A as a function of applied load. β is calculated at each load from the slope of the semilog plot of conductance versus number of carbons in the molecular chain. No trend is observed, suggesting that β does not change appreciably with applied load.

in the chain.[1] This fitting procedure was performed on the data in Figure 7A at various applied loads and plotted in Figure 7B versus applied load. No trend in the β-value with applied load is observed.

Inclusion of Adhesion in the Model. Hertzian mechanics does not include adhesive loads and is therefore an inadequate model for the experiments in this paper. To include adhesive forces, either the DMT (Derjaguin−Müller−Toporov)[24] or JKR (Johnson−Kendall−Roberts)[25] model must be used. These models are actually two limiting cases of the more general Maugis−Dugdale mechanics where the contact is either relatively stiff with long-range forces dominating adhesion (DMT) or soft with short-range adhesive forces dominating (JKR).[26] Modification of eq 9a to incorporate and compare these models is relatively simple. The only necessary adjustment is the definition of the junction load (P), which in Hertzian mechanics is purely the applied load (P_{ap}). For DMT and JKR mechanics, P is defined by the following combinations of P_{ap} and the adhesive load (P_{ad})

$$P = P_{ap} + P_{ad} \quad \text{(DMT)} \quad (10a)$$

$$P = P_{ap} + 2\left(1 + \sqrt{1 + \frac{P_{ap}}{P_{ad}}}\right)P_{ad} \quad \text{(JKR)} \quad (10b)$$

Plots of G versus P as defined for each model can be used to determine which model is more accurate in describing the mechanics of CP-AFM monolayer junctions. Figure 8 displays representative conductance data (unloading only) versus junction load for DMT and JKR mechanics and shows a definite difference between the junction loads (P) predicted by each
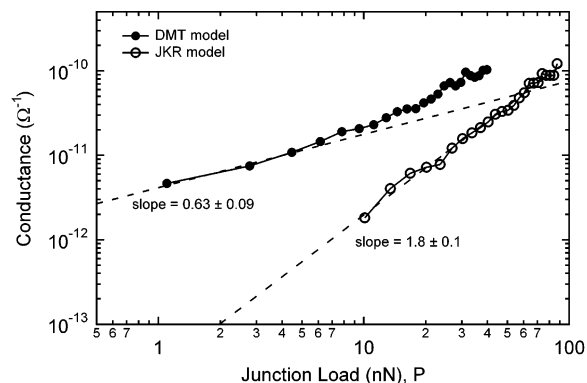
Figure 8. Representative conductance data (unloading only) for C_{10} monolayer junctions plotted versus the junction load as defined by the DMT (●, $P_{ap} + P_{ad}$) and JKR (○, $P_{ap} + 2P_{ad} + 2\sqrt{P_{ad} + P_{ap}P_{ad}}$) contact mechanics models. The conductance data is the same in each trace. The slope of the DMT trace in the low-load regime is in more agreement with the predicted slope of $2/3$ than the JKR slope.

model. The data in both traces of Figure 8 are the same; however, the conductance is plotted versus the two definitions of P from eqs 10 (i.e., for the two models). Unloading data are only considered because loading data contains plastic deformation, which is not accounted for in our equations. To assign one of the two models, we consider the slope of the data plotted on log axes (i.e., d ln(G)/d ln(P)) in the limit of small contact area. Differentiation of eq 9a following a first-order Taylor series expansion around $(a/R)^2 = 0$ yields the following predicted slope

$$\frac{d[\ln(G)]}{d[\ln(P)]} = \frac{2}{3}\left\{1 + \frac{\beta}{E^*_{film}}\left(\frac{3P}{4}\left(\frac{E^*}{R}\right)^{1/2}\right)^{2/3}\right\} \quad (11)$$

Equation 11 approaches $2/3$ for small loads. Calculation of the slope in the low-load regime for all C_{10} data provides averages of 0.78 ± 0.04 and 2.8 ± 0.2 when using the junction load (P) as defined for the DMT and JKR models, respectively. In this regard, the DMT model is in more agreement with the measured data than the JKR model. Some positive bias can be expected in the measured slope at low loads because the true slope is an increasing function of load (eq 11). Figure 8 displays power-law fits to the representative data at low loads, showing that the DMT model is in agreement with the predicted value of $2/3$ for the slope.

Two other arguments can also be made in favor of the DMT model. It has been shown by others and observed by us that the adhesive force is dependent on the applied bias between tip and substrate.[27] This suggests that the adhesion is primarily due to long-range electrostatic coupling of the tip and substrate. Nearly all of the adhesion is also completely reduced when under solvent, presumably due to electrostatic screening. Second, limiting conditions of Maugis−Dugdale mechanics are characterized in terms of an empirical unitless parameter, μ, which incorporates the adhesive force, junction stiffness, and relative size[28]

$$\mu = \left(\frac{P_{ad}^2}{4\pi^2 R E^{*2} z_0^3}\right)^{1/3} \quad (12)$$

where z_0 is a characteristic distance for the interaction potential of the contact. JKR mechanics are valid if μ is greater than 3, which is not the case ($\mu = 1.7$) for conservative values of E^* (5 GPa) and z_0 (1 Å). The adhesion force is typically ~10 nN, and the tip radius is ~20 nm. More realistic values for the

Nanoindentation and Tunneling through SAMs

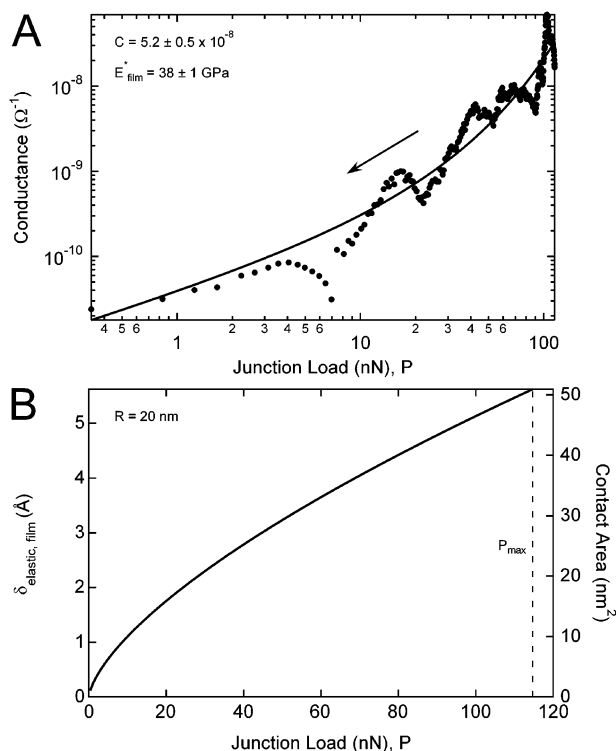*J. Phys. Chem. B, Vol. 110, No. 20, 2006* **10017**

Figure 9. (A) Plot of a representative conductance versus junction load trace (during unloading) and curve fit using eq 9a for a C_{10} monolayer. Fit parameters give estimates of the film modulus, E_{film}^* (38 GPa), and proportionality constant, C (5.2×10^{-8}). (B) Plot of elastic film deformation ($\delta_{elastic,film}$) and contact area (πa^2) calculated from eqs 6 and 7 using the data in panel A. The parameters share the same line with different axes because they have the same functional dependence on junction load.

parameters predict $\mu = 0.07$ ($E^* = 20$ GPa, $z_0 = 1$ nm), which is consistent with the DMT model. The result of these considerations is that we have used eq 10a to estimate the proper junction load to be employed in the junction conductance model (eq 9a).

Determination of Fit Parameters. Information about the mechanical properties of SAM junctions can be extrapolated from conductance versus load data according to eq 9a. In this equation, there are essentially two free parameters, the film modulus (E_{film}^*) and the proportionality constant C, as the other parameters can be assigned reasonable values ($\beta = 0.9$ Å^{-1}, $\sigma = 4.0$ nm^{-2}, $E_{tip}^* = 86$ GPa, and $R = 20$ nm). Load versus depth plots, similar to conventional nanoindentation experiments, can also be estimated. Equation 11 predicts that the conductance should scale linearly with load on log axes for small loads (Figure 8), and deviation from linearity at higher loads is determined by the value for the film modulus. Therefore, fitting of eq 9a to $G-P$ data on log axes is a good method by which the fit parameters E_{film}^* and C are decoupled. Figure 9A displays a single $G-P$ trace during unloading (P calculated assuming DMT), fit using eq 9a. The fit provides a value for E_{film}^* that is equal to 38 ± 1 GPa. This value for the modulus can then be inserted into eqs 6 and 7 to estimate the amount of elastic displacement in the film ($\delta_{elastic,film}$) and the contact area as a function of load during unloading. These calculations are displayed in Figure 9B.

Although unloading is assumed to behave essentially elastically, the loading portion of the force−distance trace contains a significant amount of plastic deformation as suggested by the hysteresis in Figure 3. Therefore, when the tip has disengaged

from the surface and zero junction load is present, the depth of the tip relative to the surface of the monolayer film is not zero (i.e., an indentation is left behind). This fact complicates our analysis, particularly regarding the contact area as calculated using eq 6a and, hence, the model equation (eq 9a). To illustrate this complication, we consider that the contact area (for the perfectly elastic case) can be expressed as a simple function of the indentation depth by combination of eqs 6a and 6b

$$a = \sqrt{R\delta} \qquad (13)$$

Therefore during unloading, the depth of the indent is greater than the elastic deformation in the film (eq 7), and it would be expected that the true contact area is greater than the value calculated from eq 6a. We have introduced this consideration into our model equation by expressing a according to eq 13 with δ equal to the sum of eq 7 and a constant value for the plastic deformation (δ_p). This weakly affects the extrapolated value of E_{film}^* (for any value δ_p) but results in poor fits to the data at low loads. Specifically, the *modeled* slope of the $G-P$ trace on log axes was much less than $^2/_3$ at low loads, even if slight values of δ_p were assumed. This is contradictory to the *observed* slope of $^2/_3$, which we believe stems from a gradual reduction of the contact area toward zero (as predicted in the elastic limit) rather than a finite value at zero junction load. Therefore, we have used eq 6a (not eq 13) as a reasonable approximation of the dependence of the contact radius on load at low loads, although the contact area is likely much larger than that calculated at high loads. Equation 9a is also accepted as adequate for determining E_{film}^*.

To estimate the amount of plastic deformation (δ_p), we assume that the primary difference between loading and unloading conductances at a particular load is an exponential factor containing the plastic deformation. In other words, the unloading conductance divided by the loading conductance (defined as the hysteresis ratio, H) is the exponential of the β-value times a function of the plastic deformation that must depend on the junction load and that must equal zero at P_{max}

$$H(P) \equiv \frac{G_{unloading}(P)}{G_{loading}(P)} \approx \exp(\beta(\delta_{plastic}(P_{max}) - \delta_{plastic}(P))) \quad (14)$$

The functional dependence of $\delta_{plastic}(P)$ is not absolutely known; however, we have chosen a power-law relation because plastic deformation is often described using power laws.[29] Therefore, eq 14 can be written as follows

$$\ln(H) \approx \beta b(P_{max}{}^n - P^n) \qquad (15a)$$

where

$$\delta_{plastic}(P_{max}) = bP_{max}{}^n \equiv \delta_{plastic} \qquad (15b)$$

Equation 15a fits the measured hysteresis ratio data well; however, there is a large amount of uncertainty in b due to the fact that n is a free fit parameter in the exponent (i.e., small perturbations in n result in large changes in b). For this reason, fits are performed using a fixed value of n (0.33), which is the average value obtained when it is allowed to vary freely. Although this introduces a systematic error, it reduces the variability in b. Figure 10A displays the hysteresis ratio for the data in Figure 9 on semilog axes and fit according to eq 15a with $P_{max} = 114$ nN and $n = 0.33$. The estimated plastic deformation for this trace at $P_{max}(\delta_p)$ is 9.3 Å. This value is then added to the elastic deformation ($\delta_{elastic,film}$) to estimate
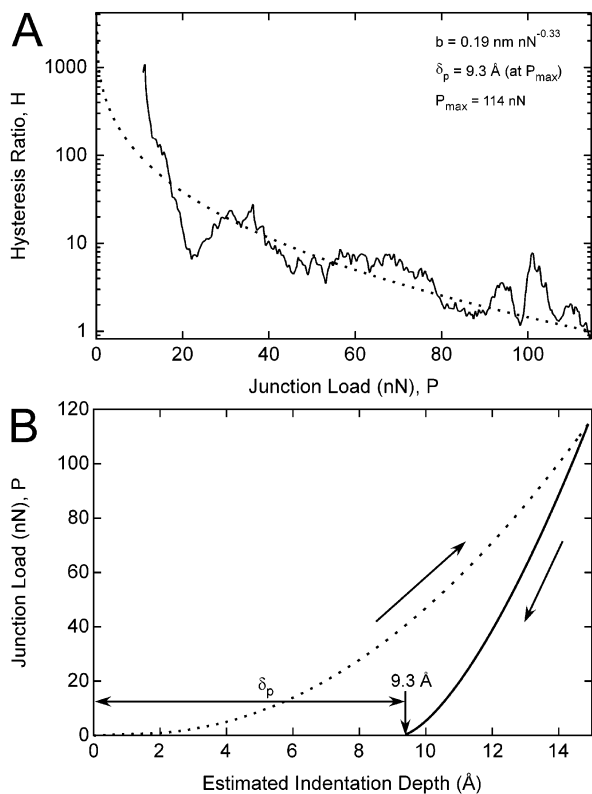
Figure 10. (A) Semilog plot of hysteresis ratio versus junction load. The dotted line represents the fit of eq 15a with $P_{max} = 114$ nN and $n = 0.33$. The plastic deformation is estimated to be 9.3 Å at the maximum junction load (δ_p). (B) Plot of junction load versus calculated probe depth for the C_{10} monolayer data in Figure 9A. The unloading trace is essentially the same as junction load versus $\delta_{elastic,film}$ shifted along the x-axis by a distance of δ_p.

TABLE 1: Calculated Parameters for Alkanethiol Monolayers as Determined by Curve Fits of Eqs 9 and 15[a]

monolayer	$E^* \pm$ (GPa)		$T_0 \pm$ ($\times 10^{-6}$)		$\delta_p \pm$ (Å)	
C_6	54	5	9	4	6.7	0.4
C_8	52	5	1.4	0.9	6.3	0.6
C_{10}	48	5	2	1	7.3	0.7
C_{12}	75	10	1.5	0.9	9.9	0.9

[a] Error values represent one standard error of the parameter.

the indentation depth of the AFM tip during unloading (Figure 10B). An estimate for the loading curve is also shown in Figure 10B as a dotted line (calculated as the sum of $\delta_{elastic,film}(P)$ and $\delta_{plastic}(P)$).[30] At first glance, it appears that the estimated value of indentation is exceedingly large (the film is only expected to be ~14 Å thick); however, it is necessary to account for the amount of hysteresis in the measurement, and it can be justified by the fact that immeasurably large currents have been observed for only slightly larger loads (~150 nN), suggesting that the film is almost completely punched through.

Finally, an estimate of the contact transmission function, T_0, can be calculated using eq 9b. The proportionality constant, C, is determined by the curve fit of $G-P$ data to eq 9a, δ_p from the hysteresis analysis, and t_0 ~14 Å for C_{10} films. For the data in Figures 6.9 and 6.10, T_0 is calculated to be $3.6 \pm 0.6 \times 10^{-6}$. Figures 6.9 and 10 provide example data for the calculation of fit parameters; however, more traces have been acquired and may be used to provide better statistical estimates of the important parameters. Table 1 lists the average and standard error for the parameters (E^*_{film}, T_0, and δ_p) that have been calculated for monolayers of C_6, C_8, C_{10}, and C_{12}. The averages are based on experiments performed with multiple tips
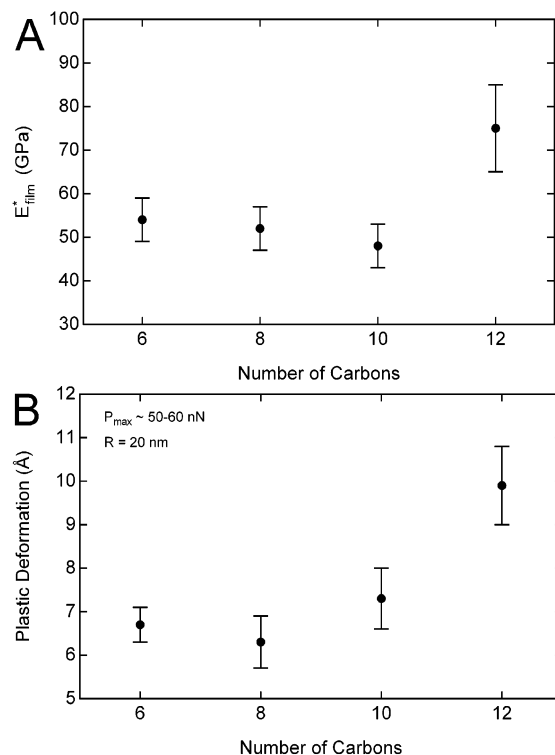

Figure 11. (A) Average film modulus, E^*_{film}, and (B) plastic deformation, δ_p, calculated for Au−alkanethiol/Au junctions. The modulus is observed to decrease with monolayer chain length for the shorter chains and abruptly reverse trend once 12 carbons are present in the chain. Plastic deformation is observed to remain relatively constant with chain length and increase for C_{12} films. This may be indicative of an inability for the C_{12} film to heal under stress as compared to the liquidlike shorter chains.

and similar values of the junction P_{max} (~50−60 nN). Approximately 50 traces are geometrically averaged into each value. Outliers have been omitted according to the Chauvenet criterion.

The data in Table 1 show a decrease in the reduced modulus with increasing chain length for the shortest three chains (C_6, C_8, and C_{10}), consistent with the fact that increasing the thickness of the film reduces the stiffness. A distinct reversal in this trend is observed between chains of C_{10} and C_{12} as the modulus increases from ~50 to 75 GPa. This is consistent with many observations that a distinct transition occurs in the phase of alkanethiol monolayers at ~12 carbons from liquidlike to very crystalline.[14] These extrapolated values are well within the range of elastic moduli reported in the literature for monolayers and similar molecular solids. Calculations predict the moduli of alkane monolayers to range between about 20−40 GPa[31] and as large as 240 GPa for single-crystalline polyethylene.[32] Experimental measurements of lattice strain under applied pressure using X-ray diffraction suggest the moduli of crystalline polypropylene and polyethylene to be as high as 40 and 240 GPa, respectively.[33] Crystals of *n*-paraffins have also exhibited large moduli >300 GPa along the molecular chain and 8−30 GPa normal to the molecular chain.[34] However, other reports suggest that the moduli of organic monolayers and highly oriented chains of polyethylene are much lower, ~0.4−3 GPa.[35]

The plastic deformation (δ_p) is estimated to be essentially constant, although accuracy in this parameter is low. It is possible that the increase at 12 carbons is attributable to the inability of the more crystalline chains to reorganize, compared to the more liquidlike short-chain monolayers. The modulus and deformation data are also graphically displayed in Figure 11.

The T_0 value is also relatively constant for the monolayers studied. Comparison of the contact transmission can be made to our previously published work in which we calculated the transmission for Au$-$S$-$C and CH$_3$/Au contacts ($T_{\text{Au}-\text{S}-\text{C}}$ and $T_{\text{CH}_3/\text{Au}}$), depending on the number of molecules estimated to be in those junctions.[1] For junction loads of $\sim$12 nN (approximately those used in ref 1), we estimate the contact area of the junctions to be about 7 nm^2, containing $\sim$30 molecules. This provides estimates for $T_{\text{Au}-\text{S}-\text{C}}$ and $T_{\text{CH}_3/\text{Au}}$ of 0.60 and 0.013, respectively. Therefore, the combined contact transmission is calculated to be 7.8×10^{-3} ($T_{\text{Au}-\text{S}-\text{C}} \times T_{\text{CH}_3/\text{Au}}$). At first glance, this does not appear to be in agreement with the values in Table 1. However, this value does not include the effects of junction compression. That is, the junction thickness prior to deformation (t_0) was used in the calculation of $T_{\text{Au}-\text{S}-\text{C}}$ and $T_{\text{CH}_3/\text{Au}}$ rather than the correct junction thickness ($t_0 - \delta_\text{p}$). This means that our previously calculated value of 7.8×10^{-3} must be reduced by a factor of $\exp(\beta\delta_\text{p})$ to agree with the values of T_0 calculated in this paper. For typical values of δ_p the correction factor is $\sim$550, yielding an estimate of T_0 of $\sim 2 \times 10^{-5}$, which is in reasonable agreement with the values in Table 6.1.

Conclusions

Electrical tunneling measurements were performed on alkanethiol monolayer junctions using CP-AFM. The junctions were created by self-assembly of alkanethiol molecules on Au-coated Si substrates, which were then contacted with a Au-coated AFM tip. Conductance of the junction was measured using external electronics that held the tip at 0.2 V relative to the grounded substrate. The CP-AFM arrangement allowed for measurement of conductance over a range of applied loads by dynamically cycling the substrate position into and out of contact with the tip. The acquired data closely resembles that of conventional nanoindentation experiments in which an ultrasharp punch is used to indent a surface and junction load is monitored as a function of indentation depth. However, in this arrangement, the junction conductance was measured rather than the indentation depth. Standard models for tunneling conductance and contact mechanics were then used to transform conductance data into penetration depth and provided estimates for the modulus of the monolayer, contact transmission function, and amount of plastic deformation.

It was concluded that a substantial amount of plastic deformation occurs when monolayers are subjected to sufficient loads under an AFM tip. Junction conductance was consistently lower during loading than unloading, suggesting that as the film was compressed, molecules were splayed into vacancies in the surrounding monolayer matrix. Upon unloading, the molecules did not return fully to their original configurations, which resulted in a thinner monolayer and significantly higher conductance than during loading. The hysteresis was observed consistently for all measurements made on alkane monolayer systems including those measurements performed under cyclohexane where adhesive forces were essentially eliminated. Hysteresis was not observed on films of Al$_2$O$_3$, which is presumably much harder than the monolayers and which therefore did not plastically deform under the same applied loads. Further indication that the monolayers were deformed plastically stemmed from the dependence of the hysteresis on maximum applied load and the lack of dependence on loading rate. More hysteresis was observed for measurements that were carried out to higher maximum applied loads where larger amounts of plastic deformation occurred. The amount of

hysteresis also did not depend on the loading$-$unloading rate, suggesting that the conductance was not affected in a time-dependent fashion, which would have been indicative of viscoelastic deformation or capacitive charging.

To properly discuss the contact mechanics of the monolayer junctions, adhesive forces were included according to the DMT model. In this model, the junction load was determined by the sum of the adhesive load (the applied load at pull-off) and the applied load. This model was chosen because the slope of the conductance$-$load trace on log axes approached the expected value of $^2/_3$ at small loads for this definition of junction load. The slope as determined with the JKR definition of junction load (eq 10b) did not approach $^2/_3$. The adhesion was also observed to be dependent on the junction bias and was nearly eliminated by the presence of cyclohexane. These observations suggested that the adhesion was predominantly electrostatic in nature, consistent with the long-range nature of adhesion forces in DMT mechanics.

Unloading data for conductance versus junction load were curve-fit according to a model that incorporated dependences on contact area and monolayer compression. The conductance was assumed to scale linearly with the contact area and exponentially on the thickness of the film. These parameters were defined as functions of the DMT junction load using equations from Hertzian contact mechanics. The curve fit was a simple two-independent-parameter fit where the scaling was determined by the contact transmission, and the curvature on log axes was determined by the monolayer modulus. Finally, the penetration depth of the AFM tip was determined by analysis of the hysteresis between loading and unloading conductances. Assuming a simple power-law relation between plastic deformation and junction load, estimates were calculated for the amount of plastic deformation in the films. The plastic deformation, film modulus, and contact transmission were compared for junctions of C$_6$, C$_8$, C$_{10}$, and C$_{12}$.

The film modulus was shown to decrease slightly for the shorter chains containing C$_6$$-C_{10}$ (54$-$48 GPa) and significantly increase for the longest chain measured, C$_{12}$ (75 GPa). The decrease in modulus with increasing chain length (for the shorter chains) is consistent with the expected reduction in stiffness of thicker films. The drastic reversal in this trend observed between the stiffness of the shorter chains and C$_{12}$ is indicative of the change in phase reported to exist between these chain lengths.[14] The C$_{12}$ molecules are packed considerably tighter than shorter-chain molecules. The final depth of penetration was shown to be essentially constant at $\sim$7 Å. The contact transmission was also determined to be essentially constant ($\sim 2 \times 10^{-6}$). The value of contact transmission for the shorter chains was consistent with previously reported values assuming that approximately 30 molecules were probed at 2 nN of applied load and that the films were compressed by about 7 Å.

References and Notes

(1) Engelkes, V. B.; Beebe, J. M.; Frisbie, C. D. *J. Am. Chem. Soc.* **2004**, *126*, 14287$-$14296.

(2) (a) Kushmerick, J. G.; Lazorcik, J.; Patterson, C. H.; Shashidhar, R.; Seferos, D. S.; Bazan, G. C. *Nano Lett.* **2004**, *4*, 639$-$642. (b) Lee, T.; Wang, W.; Klemic, J. F.; Zhang, J. J.; Su, J.; Reed, M. A. *J. Phys. Chem. B* **2004**, *108*, 8742$-$8750. (c) Liu, B.; Bard, A. J.; Mirkin, M. V.; Creager, S. E. *J. Am. Chem. Soc.* **2004**, *126*, 1485$-$1492. (d) Weiss, E. A.; Ahrens,

M. J.; Sinks, L. E.; Gusev, A. V.; Ratner, M. A.; Wasielewski, M. R. *J. Am. Chem. Soc.* **2004**, *126*, 5577−5584. (e) Kushmerick, J. G.; Naciri, J.; Yang, J. C.; Shashidhar, R. *Nano Lett.* **2003**, *3*, 897−900. (f) Ramachandran, G. K.; Tomfohr, J. K.; Li, J.; Sankey, O. F.; Zarate, X.; Primak, A.; Terazono, Y.; Moore, T. A.; Moore, A. L.; Gust, D.; Nagahara, L. A.; Lindsay, S. M. *J. Phys. Chem. B* **2003**, *107*, 6162−6169. (g) Salomon, A.; Cahen, D.; Lindsay, S.; Tomfohr, J.; Engelkes, V. B.; Frisbie, C. D. *Adv. Mater.* **2003**, *15*, 1881−1890. (h) Chabinyc, M. L.; Chen, X.; Holmlin, R. E.; Jacobs, H.; Skulason, H.; Frisbie, C. D.; Mujica, V.; Ratner, M. A.; Rampi, M. A.; Whitesides, G. M. *J. Am. Chem. Soc.* **2002**, *124*, 11730−11736. (i) Cui, X. D.; Primak, A.; Zarate, X.; Tomfohr, J.; Sankey, O. F.; Moore, A. L.; Moore, T. A.; Gust, D.; Nagahara, L. A.; Lindsay, S. M. *J. Phys. Chem. B* **2002**, *106*, 8609−8614. (j) Kushmerick, J. G.; Holt, D. B.; Yang, J. C.; Naciri, J.; Moore, M. H.; Shashidhar, R. *Phys. Rev. Lett.* **2002**, *89*, 086802. (k) Selzer, Y.; Salomon, A.; Cahen, D. *J. Am. Chem. Soc.* **2002**, *124*, 2886−2887. (l) Chabinyc, M. L.; Chen, X.; Holmlin, R. E.; Jacobs, H. O.; Rampi, M. A.; Whitesides, G. M. *Abstr. Pap. Am. Chem. Soc.* **2001**, *221*, COLL-009. (m) Holmlin, R. E.; Haag, R.; Chabinyc, M. L.; Ismagilov, R. F.; Cohen, A. E.; Terfort, A.; Rampi, M. A.; Whitesides, G. M. *J. Am. Chem. Soc.* **2001**, *123*, 5075−5085. (n) Hong, S.; Reifenberger, R.; Tian, W.; Datta, S.; Henderson, J.; Kubiak, C. P. *Superlattices Microstruct.* **2000**, *28*, 289−303. (o) Wold, D. J.; Frisbie, C. D. *J. Am. Chem. Soc.* **2000**, *122*, 2970−2971. (p) Bumm, L. A.; Arnold, J. J.; Dunbar, T. D.; Allara, D. L.; Weiss, P. S. *J. Phys. Chem. B* **1999**, *103*, 8122−8127. (q) Slowinski, K.; Slowinska, K. U.; Majda, M. *J. Phys. Chem. B* **1999**, *103*, 8544−8551. (r) Bumm, L. A.; Arnold, J. J.; Cygan, M. T.; Dunbar, T. D.; Burgin, T. P.; Jones, L., II.; Allara, D. L.; Tour, J. M.; Weiss, P. S. *Science* **1996**, *271*, 1705−1707. (s) Slowinski, K.; Chamberlain, R. V., II.; Bilewicz, R.; Majda, M. *J. Am. Chem. Soc.* **1996**, *118*, 4709−4710. (t) Polymeropoulos, E. E.; Sagiv, J. *J. Chem. Phys.* **1978**, *69*, 1836−1847.

(3) (a) Wang, W.; Lee, T.; Reed, M. A. *Phys. Rev. B* **2003**, *68*, 035416. (b) Holmlin, R. E.; Ismagilov, R. F.; Haag, R.; Mujica, V.; Ratner, M. A.; Rampi, M. A.; Whitesides, G. M. *Angew. Chem., Int. Ed.* **2001**, *40*, 2316−2320. (c) Wold, D. J.; Frisbie, C. D. *J. Am. Chem. Soc.* **2001**, *123*, 5549−5556. (d) Slowinski, K.; Fong, H. K. Y.; Majda, M. *J. Am. Chem. Soc.* **1999**, *121*, 7257−7261.

(4) Beebe, J. M.; Engelkes, V. B.; Miller, L. L.; Frisbie, C. D. *J. Am. Chem. Soc.* **2002**, *124*, 11268−11269.

(5) Cui, X. D.; Zarate, X.; Tomfohr, J.; Sankey, O. F.; Primak, A.; Moore, A. L.; Moore, T. A.; Gust, D.; Harris, G.; Lindsay, S. M. *Nanotechnology* **2002**, *13*, 5−14.

(6) Kushmerick, J. G.; Holt, D. B.; Pollack, S. K.; Ratner, M. A.; Yang, J. C.; Schull, T. L.; Naciri, J.; Moore, M. H.; Shashidhar, R. *J. Am. Chem. Soc.* **2002**, *124*, 10654−10655.

(7) (a) Selzer, Y.; Salomon, A.; Cahen, D. *J. Phys. Chem. B* **2002**, *106*, 10432−10439. (b) Wold, D. J.; Haag, R.; Rampi, M. A.; Frisbie, C. D. *J. Phys. Chem. B* **2002**, *106*, 2813−2816. (c) Cui, X. D.; Primak, A.; Zarate, X.; Tomfohr, J.; Sankey, O. F.; Moore, A. L.; Moore, T. A.; Gust, D.; Harris, G.; Lindsay, S. M. *Science* **2001**, *294*, 571−574. (d) Slowinski, K.; Chamberlain, R. V.; Miller, C. J.; Majda, M. *J. Am. Chem. Soc.* **1997**, *119*, 11910−11919.

(8) Zhou, C.; Muller, C. J.; Deshpande, M. R.; Sleight, J. W.; Reed, M. A. *Appl. Phys. Lett.* **1995**, *67*, 1160−1162.

(9) (a) Beebe, J. M.; Engelkes, V. B.; Liu, J.; Gooding, J. J.; Eggers, P. K.; Jun, Y.; Zhu, X.; Paddon-Row: M. N.; Frisbie, C. D. *J. Phys. Chem. B* **2005**, *109*, 5207−5215. (b) Kondo, M.; Tada, T.; Yoshizawa, K. *J. Phys. Chem. A* **2004**, *108*, 9143−9149.

(10) (a) Tomfohr, J. K.; Sankey, O. F. *Phys. Rev. B* **2002**, *65*, 245105. (b) Leatherman, G.; Durantini, E. N.; Gust, D.; Moore, T. A.; Moore, A. L.; Stone, S.; Zhou, Z.; Rez, P.; Liu, Y. Z.; Lindsay, S. M. *J. Phys. Chem. B* **1999**, *103*, 4006−4010.

(11) (a) Seminario, J. M.; De La Cruz, C. E.; Derosa, P. A. *J. Am. Chem. Soc.* **2001**, *123*, 5616−5617. (b) Yaliraki, S. N.; Ratner, M. A. *J. Chem. Phys.* **1998**, *109*, 5036−5043.

(12) Zhou, C.; Deshpande, M. R.; Reed, M. A.; Jones, K., II. ; Tour, J. M. *Appl. Phys. Lett.* **1997**, *71*, 611−613.

(13) (a) Xiao, X.; Nagahara, L. A.; Rawlett, A. M.; Tao, N. *J. Am. Chem. Soc.* **2005**, *127*, 9235−9240. (b) Xu, B.; Xiao, X.; Yang, X.; Zang, L.; Tao, N. *J. Am. Chem. Soc.* **2005**, *127*, 2386−2387.

(14) (a) Ulman, A. *Characterization of Organic Thin Films*; Butterworth-Heinemann: Boston, 1995. (b) Camillone, N., III.; Chidsey, C. E. D.; Liu, G. Y.; Putvinski, T. M.; Scoles, G. *J. Chem. Phys.* **1991**, *94*, 8493−8502. (c) Porter, M. D.; Bright, T. B.; Allara, D. L.; Chidsey, C. E. D. *J. Am. Chem. Soc.* **1987**, *109*, 3559−3568.

(15) Blackstock, J. J.; Li, Z.; Freeman, M. R.; Stewart, D. R. *Surf. Sci.* **2003**, *546*, 87−96.

(16) Levy, R.; Maalmoum, M. *Nanotechnology* **2002**, *13*, 33−37.

(17) Stark, R. W.; Drobek, T.; Heckl, W. M. *Ultramicroscopy* **2001**, *86*, 207−215.

(18) Schneider, J.; Dori, Y.; Haverstick, K.; Tirrell, M.; Sharma, R. *Langmuir* **2002**, *18*, 2702−2709.

(19) (a) Kiely, J. D.; Houston, J. E.; Mulder, J. A.; Hsung, R. P.; Zhu, X. Y. *Tribol. Lett.* **2000**, *7*, 103−107. (b) Joyce, S. A.; Thomas, R. C.; Houston, J. E.; Michalske, T. A.; Crooks, R. M. *Phys. Rev. Lett.* **1992**, *68*, 2790−2793.

(20) Petersen, K. E. *Proc. IEEE* **1982**, *70*, 420−457.

(21) (a) Field, J. S.; Swain, M. V. *J. Mater. Res.* **1993**, *8*, 297−306. (b) Bell, T. J.; Field, J. S.; Swain, M. V. *Thin Solid Films* **1992**, *220*, 289−294. (c) Oliver, W. C.; Pharr, G. M. *J. Mater. Res.* **1992**, *7*, 1564−1583. (d) Bell, T. J.; Bendeli, A.; Field, J. S.; Swain, M. V.; Thwaite, E. G. *Metrologia* **1991/1992**, *28*, 463−469. (e) Doerner, M. F.; Nix, W. D. *J. Mater. Res.* **1986**, *1*, 601−609.

(22) Landauer, R. *Phys. Lett. A* **1981**, *85*, 91−93.

(23) Johnson, K. L. *Contact Mechanics*; Cambridge University Press: New York, 1987.

(24) (a) Müller, V. M.; Derjaguin, B. V.; Toporov, Y. P. *Colloids Surf.* **1983**, *7*, 251−259. (b) Derjaguin, B. V.; Müller, V. M.; Toporov, Y. P. *J. Colloid Interface Sci.* **1975**, *53*, 314−326.

(25) Johnson, K. L.; Kendall, K.; Roberts, A. D. *Proc. R. Soc. London, Ser. A* **1971**, *324*, 301−313.

(26) Maugis, D. *J. Colloid Interface Sci.* **1992**, *150*, 243−269.

(27) Tivanski, A. V.; Bemis, J. E.; Akhremitchev, B. B.; Liu, H.; Walker, G. C. *Langmuir* **2003**, *19*, 1929−1934.

(28) Johnson, K. L. *Proc. R. Soc. London, Ser. A* **1997**, *453*, 163−179.

(29) Hu, X. Z.; Lawn, B. R. *Thin Solid Films* **1998**, *322*, 225−232.

(30) Loading trace: Depth $= bP^n + E^*/E^*_{film}(9/16R)^{1/3}(1/E^*)^{2/3}P^{2/3}$. Unloading trace: Depth $= \delta_p + E^*/E^*_{film}(9/16R)^{1/3}(1/E^*)^{2/3}P^{2/3}$.

(31) (a) Leng, Y.; Jiang, S. *J. Chem. Phys.* **2000**, *113*, 8800−8806. (b) Siepmann, J. I.; McDonald, I. R. *Phys. Rev. Lett.* **1993**, *70*, 453−456.

(32) Anand, J. N. *J. Macromol. Sci., Part B* **1967**, *1*, 445−458.

(33) Sakurada, I.; Nukushina, Y.; Ito, T. *J. Polym. Sci.* **1962**, *57*, 651−660.

(34) Muller, A. *Proc. R. Soc. London, Ser. A* **1941**, *178*, 227−241.

(35) (a) Bartczak, Z.; Morawiec, J.; Galeski, A. *J. Appl. Polym. Sci.* **2002**, *86*, 1405−1412. (b) Overney, R. M.; Meyer, E.; Frommer, J.; Guentherodt, H. J.; Fujihira, M.; Takano, H.; Gotoh, Y. *Langmuir* **1994**, *10*, 1281−1286. (c) Salmeron, M.; Neubauer, G.; Folch, A.; Tomitori, M.; Ogletree, D. F.; Sautet, P. *Langmuir* **1993**, *9*, 3600−3611.